# Inelastic scattering of neutron-rich Ni and Zn isotopes off a proton target

M. L. Cortés,[1,2,*] P. Doornenbal,[3] M. Dupuis,[4] S. M. Lenzi,[5] F. Nowacki,[6] A. Obertelli,[7,3] S. Péru,[4] N. Pietralla,[1] V. Werner,[1] K. Wimmer,[8] G. Authelet,[7] H. Baba,[3] D. Calvet,[7] F. Château,[7] A. Corsi,[7] A. Delbart,[7] J-M. Gheller,[7] A. Gillibert,[7] T. Isobe,[3] V. Lapoux,[7] C. Louchart,[1] M. Matsushita,[9] S. Momiyama,[3,8] T. Motobayashi,[3] M. Niikura,[8] H. Otsu,[3] C. Péron,[7] A. Peyaud,[7] E. C. Pollacco,[7] J-Y. Roussé,[7] H. Sakurai,[3,8] C. Santamaria,[8] M. Sasano,[3] Y. Shiga,[3,10] S. Takeuchi,[3] R. Taniuchi,[3,8] T. Uesaka,[3] H. Wang,[3] K. Yoneda,[3] F. Browne,[3,11] L. X. Chung,[12] Zs. Dombradi,[13] S. Franchoo,[14] F. Giacoppo,[2,15,16] A. Gottardo,[14] K. Hadynska-Klek,[17,15] Z. Korkulu,[13] S. Koyama,[3,8] Y. Kubota,[3,9] J. Lee,[18] M. Lettmann,[1] R. Lozeva,[6,19] K. Matsui,[3,8] T. Miyazaki,[3,8] S. Nishimura,[3] L. Olivier,[14] S. Ota,[9] Z. Patel,[20] E. Sahin,[15] C. M. Shand,[20] P-A. Söderström,[3] I. Stefan,[14] D. Steppenbeck,[9] T. Sumikama,[21] D. Suzuki,[14] Zs. Vajta,[13] J. Wu,[3,22] and Z. Xu[18]

[1]*Institut für Kernphysik, Technische Universität Darmstadt, 64289 Darmstadt, Germany*
[2]*GSI Helmoltzzentrum für Schwerionenforschung GmbH, 64291 Darmstadt, Germany*
[3]*RIKEN Nishina Center, 2-1 Hirosawa, Wako, Saitama 351-0198, Japan*
[4]*CEA, DAM, DIF, F-91297 Arpajon, France*
[5]*Dipartimento di Fisica e Astronomia, Università di Padova and INFN, Sezione di Padova, Via F. Marzolo 8, I-35131 Padova, Italy*
[6]*IPHC, CNRS/IN2P3, Université de Strasbourg, F-67037 Strasbourg, France*
[7]*IRFU, CEA, Université Paris-Saclay, F-91191 Gif-sur-Yvette, France*
[8]*Department of Physics, University of Tokyo, 7-3-1 Hongo, Bunkyo, Tokyo 113-0033, Japan*
[9]*Center for Nuclear Study, University of Tokyo, RIKEN campus, Wako, Saitama 351-0198, Japan*
[10]*Department of Physics, Rikkyo University, 3-34-1 Nishi-Ikebukuro, Toshima, Tokyo 172-8501, Japan*
[11]*School of Computing Engineering and Mathematics, University of Brighton, Brighton BN2 4GJ, United Kingdom*
[12]*Institute for Nuclear Science & Technology, VINATOM, 179 Hoang Quoc Viet, Cau Giay, Hanoi, Vietnam*
[13]*MTA Atomki, P. O. Box 51, Debrecen H-4001, Hungary*
[14]*Institut de Physique Nucléaire Orsay, IN2P3-CNRS, 91406 Orsay Cedex, France*
[15]*Department of Physics, University of Oslo, N-0316 Oslo, Norway*
[16]*Helmholtz Institute Mainz, 55099 Mainz, Germany*
[17]*Istituto Nazionale di Fisica Nucleare, Laboratori Nazionali di Legnaro, Viale dell'Università, 2, I-35020 Legnaro, Italy*
[18]*Department of Physics, The University of Hong Kong, Pokfulam, Hong Kong*
[19]*CSNSM, CNRS/IN2P3, Université Paris-Sud, F-91405 Orsay Campus, France*
[20]*Department of Physics, University of Surrey, Guildford GU2 7XH, United Kingdom*
[21]*Department of Physics, Tohoku University, Sendai 980-8578, Japan*
[22]*State Key Laboratory of Nuclear Physics and Technology, Peking University, Beijing 100871, People's Republic of China*

(Received 23 May 2017; revised manuscript received 17 November 2017; published 19 April 2018)

Proton inelastic scattering of $^{72,74}$Ni and $^{76,80}$Zn ions at energies around 235 MeV/nucleon was performed at the Radioactive Isotope Beam Factory and studied using $\gamma$-ray spectroscopy. Angular integrated cross sections for direct inelastic scattering to the $2_1^+$ and $4_1^+$ states were measured. The Jeukenne-Lejeune-Mahaux folding model, extended beyond 200 MeV, was used together with neutron and proton densities stemming from quasiparticle random-phase approximation (QRPA) calculations to interpret the experimental cross sections and to infer neutron to proton matrix element ratios. In addition, coupled-channels calculations with a phenomenological potential were used to determine deformation lengths. For the Ni isotopes, correlations favor neutron excitations, thus conserving the $Z = 28$ gap. A dominance of proton excitation, on the other hand, is observed in the Zn isotopes, pointing to the conservation of the $N = 50$ gap approaching $^{78}$Ni. These results are in agreement with QRPA and large-scale shell-model calculations.

DOI: 10.1103/PhysRevC.97.044315

## I. INTRODUCTION

Recent experimental studies have exploited the use of radioactive ion beams to gain a deeper understanding of the structure of nuclei under extreme isospin conditions. One of the most important results achieved is that the shell closures, which give rise to the magic numbers 2, 8, 20, 28, 50, 82, and 126 near the line of $\beta$ stability, change with varying number of protons and neutrons [1]. This so-called shell-evolution has been widely studied, in particular on the neutron-rich side of the nuclear chart. Experimental evidence suggests the appearance of new magic neutron numbers at $N = 32,34$ in Ca isotopes

*Present address: RIKEN Nishina Center, 2-1 Hirosawa, Wako, Saitama 351-0198, Japan; liliana@ribf.riken.jp

 

[2–4], although interpretation is still under debate [5]. A new magic number $N = 16$ has also been proposed [6–8], while there is experimental evidence of the disappearance of the shell closure at $N = 8$ [9–12], $N = 20$ [13,14], and $N = 28$ [15,16] in various neutron-rich isotopes. The next magic number, $N = 50$, is still under investigation and its possible weakening or disappearance, particularly around $^{78}$Ni, is of current interest in nuclear structure as well as in astrophysics, as it is related to the waiting points of the rapid neutron-capture process [17]. In spite of the great interest in $^{78}$Ni, direct evidence of its magicity is still unavailable. Different theoretical predictions suggest a weakening of the $Z = 28$ proton gap when approaching the $N = 50$ neutron shell closure [18], as well as the already confirmed inversion of the $\pi p_{3/2}$ and $\pi f_{5/2}$ proton single-particle energy levels [19,20]. More recent calculations suggest the appearance of a new island of inversion at $N = 50$ for isotopes with $Z \leqslant 26$ [21].

For isotopes with open shells, quadrupole correlations give rise to collectivity. Therefore, shell evolution near magic numbers can be studied by evaluating the degree of quadrupole collectivity, which is related to the quadrupole deformation parameter, $\beta_2$. These quantities can be obtained by measuring the transition probability between the ground state and the $2_1^+$ state using either electromagnetic or hadronic probes [22]. Measurements of electromagnetic strengths provide access only to the proton transition matrix element but not to the neutron counterparts. However, the contribution of the neutrons to the collectivity, and, more importantly, the ratio between proton and neutron matrix elements, becomes particularly relevant to characterize isotopes with single proton or neutron closed shells [23–25]. Therefore, it is desirable to perform measurements that allow us to probe both nucleons, such as proton inelastic scattering.

For the case of the Ni isotopic chain, the reduced transition probability, $B(E2)\uparrow = B(E2; 0_{\rm gs}^+ \rightarrow 2_1^+)$, measured between $N = 28$ and $N = 40$, shows a parabolic trend which indicates a subshell closure at $N = 40$ [26]. A measurement of the $B(E2)\uparrow$ value of $^{70}$Ni reported an enhanced collectivity for $N = 42$ [27]. This was claimed to indicate a possible weakening of the $Z = 28$ gap towards $^{78}$Ni. In contrast to this result, recent measurements on $^{72,74}$Ni [28,29] show a reduced $B(E2)\uparrow$ value for these isotopes, which would corroborate the magic character of the $N = 50$ and $Z = 28$ shell gaps. For the $N = 50$ isotones between $Z = 30$ and $Z = 40$, previously reported Coulomb excitation measurements show no indication of a reduction in the $N = 50$ shell gap at $Z = 30$ [30,31].

The present work reports on proton inelastic scattering of isotopes in the vicinity of $^{78}$Ni, namely $^{72,74}$Ni and $^{76,80}$Zn, using a thick liquid hydrogen target at energies above 200 MeV/nucleon in inverse kinematics. Section II describes the experimental set up. Section III gives the details on the extraction of the cross sections. In Sec. IV, the interpretation of the experimental cross sections in terms of a microscopic and a phenomenological reaction models is presented. Section V is dedicated to the discussions of the results obtained. The summary and perspectives of this work are given in Sec. VI.

## II. EXPERIMENTAL DETAILS

The experiment was performed at the Radioactive Isotope Beam Factory, operated by the RIKEN Nishina Center and the Center for Nuclear Study of the University of Tokyo. A $^{238}$U primary ion beam with an energy of 345 MeV/nucleon and an average intensity of 12 pnA impinged on a 3-mm-thick $^{9}$Be target at the entrance of the BigRIPS separator [32]. The fragments of interest were selected using the $B\rho$-$\Delta E$-$B\rho$ technique using two wedge-shaped aluminium degraders of 8 and 2 mm situated at the dispersive focal planes of BigRIPS. The ions were identified on an event-by-event basis by an energy loss measurement in an ionization chamber, position and angle measurements performed using parallel plate avalanche counters at different focal planes, and the time-of-flight measured between two plastic scintillators placed 46.5 m apart. Two different settings were applied to BigRIPS. From the first one, centered on $^{73}$Co, the isotopes $^{72,74}$Ni and $^{76}$Zn were analyzed, and from the second, centered on $^{79}$Cu, $^{80}$Zn was analyzed. Due to the existence of an isomeric state of $^{78}$Zn [33], $(p, p')$ cross sections could not be determined for this isotope.

The ions were focused on the MINOS device [34], composed of a 102(1)-mm-long liquid hydrogen target surrounded by a Time Projection Chamber (TPC) and placed at the entrance of the ZeroDegree spectrometer [32]. The liquid hydrogen was kept at a temperature of 20 K, resulting in a target thickness of 735(8) mg/cm$^2$. The entrance and exit windows were made of mylar and had a combined thickness of 275 $\mu$m. Pressure differences resulted in a 2-mm deformation of the entrance window, which was measured and taken into account in the analysis. MINOS was designed to track $(p, 2p)$ reactions. For the case of $(p, p')$ reactions, the energies of the scattered protons were such that they were predominantly stopped in the target before reaching the TPC. Therefore, a very low efficiency was achieved. For this reason, the information of the TPC was not used in the present analysis. The lack of information from the TPC introduced an uncertainty on the position, as well as in the velocity of the particle at the moment of $\gamma$ decay. Both factors affected the Doppler correction significantly. A typical resolution [full width at half maximum (FWHM)] obtained using the full capabilities of MINOS is around 9% for 1 MeV gamma rays, while resolutions on the order of 14% were obtained in the present study, where the decay was assumed to occur at the center of the target. Examples of the performance of MINOS can be found in Refs. [35,36].

Behind the target, reaction products were identified using the ZeroDegree spectrometer using the same technique as in BigRIPS. Deexcitation $\gamma$ rays were detected with the DALI2 array [37], which surrounded the MINOS target. It consisted of 186 NaI(Tl) detectors covering angles from 7° to 115° (integrated along the target length) relative to the beam axis. Standard $^{60}$Co, $^{88}$Y, and $^{137}$Cs sources were used to perform the energy calibration. The full-energy-peak efficiency of the array was determined using a detailed Geant4 [38] simulation and was found to be 14% at 1.33 MeV with an energy resolution of 6.2% (FWHM) for a stationary source. It was necessary to use

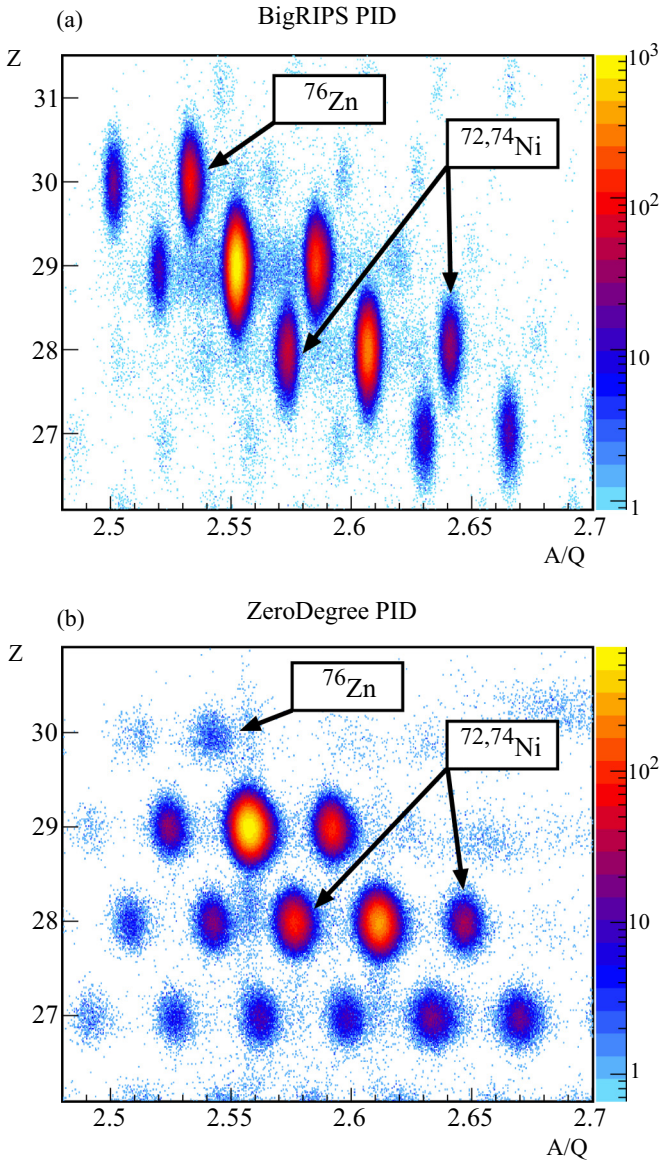


FIG. 1. Particle identification plot obtained for (a) the incoming ions, performed with the BigRIPS separator, and (b) the outgoing fragments, measured with the ZeroDegree spectrometer, for the first setting. In each case, $10^6$ events were used to make the plot. The isotopes of interest ($^{72,74}$Ni and $^{76}$Zn for this setting) are clearly identified by both spectrometers.

a simulation for determining the efficiency of the array due to the extended size of the target. Previously reported efficiency values were in agreement ($\leqslant$6% error) with the simulation [39–41].

Figure 1 shows as an example the particle identification plot obtained with the BigRIPS and ZeroDegree spectrometers for the first setting. A sample of $10^6$ events is shown. The number of $(p,p')$ events was determined as the number of ions identified event by event both in BigRIPS and ZeroDegree. As particle losses due to secondary reactions were not be identified in the ZeroDegree spectrometer, which provided the trigger, the transmission did not affect the cross-section measurements. Table I shows the total number of ions measured in the $(p,p')$ channel for each isotope under consideration as well as the average values of their energy at the entrance and exit of the target.

TABLE I. Total number of ions in the $(p,p')$ channel and energy in front ($E_{in}$) and at the exit ($E_{out}$) of the MINOS target for each of the isotopes of interest.

| Isotope | $^{72}$Ni | $^{74}$Ni | $^{76}$Zn | $^{80}$Zn |
|---|---|---|---|---|
| Number of ions | 5 018 715 | 1 619 460 | 159 030 | 9 571 520 |
| $E_{in}$ (MeV/$u$) | 271.0 | 263.5 | 275.5 | 263.4 |
| $E_{out}$ (MeV/$u$) | 205.3 | 198.3 | 204.3 | 193.8 |

## III. RESULTS

Doppler-corrected $\gamma$-ray energy spectra corresponding to the $(p,p')$ channel of the isotopes of interest were obtained assuming that the decay occurred at the center of the target and using the velocity of the ions at this position. These velocities were obtained on an event-by-event basis from the velocity measured in the ZeroDegree spectrometer plus a constant offset obtained using a LISE++ simulation [42], which took into account the energy lost by the ions in the target and in the different detectors along the beam line. In order to improve the peak-to-total ratio and the detection efficiency, the energies of $\gamma$ ray deposited in neighboring detectors, up to 15 cm, were added back.

The histograms in Fig. 2 show the spectra obtained for $^{72,74}$Ni, as well as their partial level schemes. The $2_1^+ \rightarrow 0_{gs}^+$ and $4_1^+ \rightarrow 2_1^+$ transitions were observed at 1100(5) keV and 850(3) keV for $^{72}$Ni, and 1029(7) keV and 744(3) keV for $^{74}$Ni, in agreement with the adopted values [43]. In order to extract the cross sections, each $\gamma$-ray spectrum was fitted with the simulated response of DALI2 to the $2_1^+ \rightarrow 0_{gs}^+$ transition (solid red line) and the $4_1^+ \rightarrow 2_1^+ \rightarrow 0_{gs}^+$ cascade (solid green line). To properly describe the spectra, three additional transitions at higher energies were also considered in the fit (dashed lines). A double exponential function was used to model the low-energy atomic background and the high-energy background from other sources such as reactions of scattered protons (dashed black line). The exponential function describing the atomic background was chosen the same for all the isotopes, scaled with the number of incident ions and the square of the projectile charge.

For $^{72}$Ni, the transition at 2210(15) keV is consistent with the decay of a recently reported candidate for a $2_2^+$ state [44]. Such a state was reported to have $\gamma$ ray at 1125 keV for the $2_2^+ \rightarrow 2_1^+$ decay and at 2220 keV for the $2_2^+ \rightarrow 0_{gs}^+$ decay. The presence of such a state is confirmed by the coincidence analysis shown in Fig. 3: The events in the gate between 1020 and 1100 keV are in coincidence with the $4_1^+ \rightarrow 2_1^+$ transition. When the gate is placed at 1100–1170 keV, corresponding to the $2_2^+ \rightarrow 2_1^+$ decay, the spectrum shows to be coincident with the $2_1^+ \rightarrow 0_{gs}^+$ transition. The feeding of this state was taken into account by using the reported branching ratio of 67(11)% to the $2_2^+ \rightarrow 2_1^+$ and 33(6)% to the $2_2^+ \rightarrow 0_{gs}^+$ decays [44]. Due to

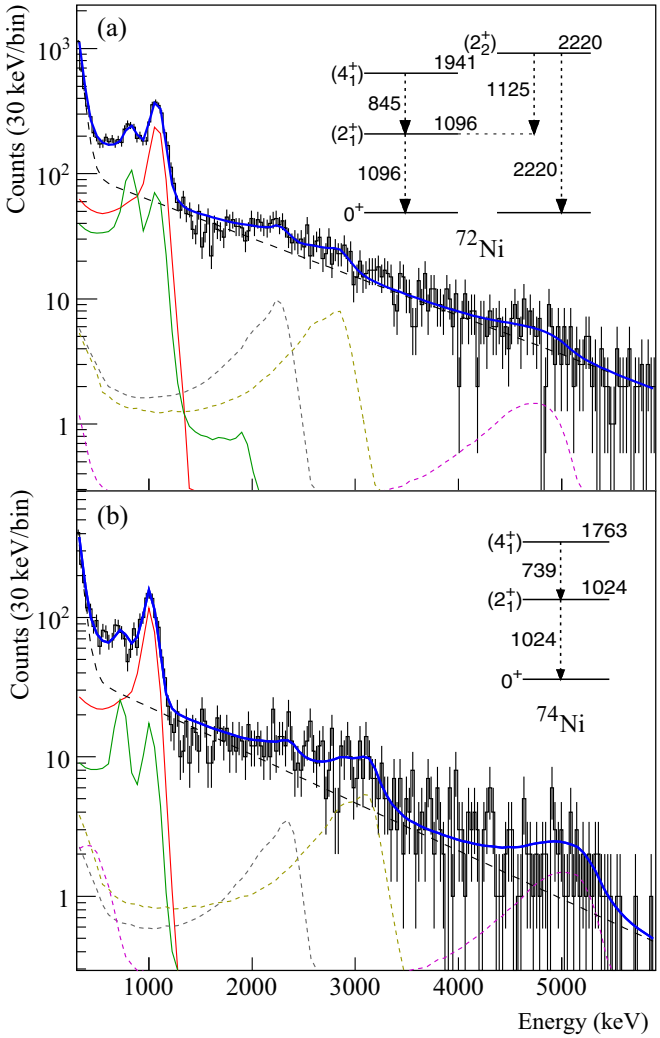


FIG. 2. Doppler corrected spectra obtained for (a) $^{72}$Ni and (b) $^{74}$Ni. Each spectrum was fitted by the convolution of the simulated response of DALI2 to the $2_1^+ \rightarrow 0_{gs}^+$ transition (solid red line) and the $4_1^+ \rightarrow 2_1^+ \rightarrow 0_{gs}^+$ cascade (solid green lines), a double exponential function which models the background (long dashed black line) and three additional transitions (dashed lines) used to obtain a better fit to the data. Levels and decay energies are taken from Refs. [43,44]. See text for details.

the similar structure of $^{72}$Ni and $^{74}$Ni, it is reasonable to assume that the line at 2242(63) keV fitted for $^{74}$Ni corresponds to the decay of a $2_2^+$ state. The energy resolution of DALI2 and limited statistics for this isotope did not allow for the unambiguous identification of this decay. Although no such state has been reported, following the case of $^{72}$Ni, we assume feeding from this state to the $2_1^+$ state, with the same values for the branching ratios.

The line at around 3000 keV fitted for both isotopes could correspond to a $3^-$ state, which is usually populated by proton inelastic scattering. The fitted energies, 2825(44) keV for $^{72}$Ni and 3120(38) keV for $^{74}$Ni, are consistent with the $3^- \rightarrow 0_{gs}^+$ decay of lighter Ni isotopes [43]. However, the energy resolution of DALI2 and the low statistics did not allow us to clearly separate these transitions or perform a coincidence analysis.

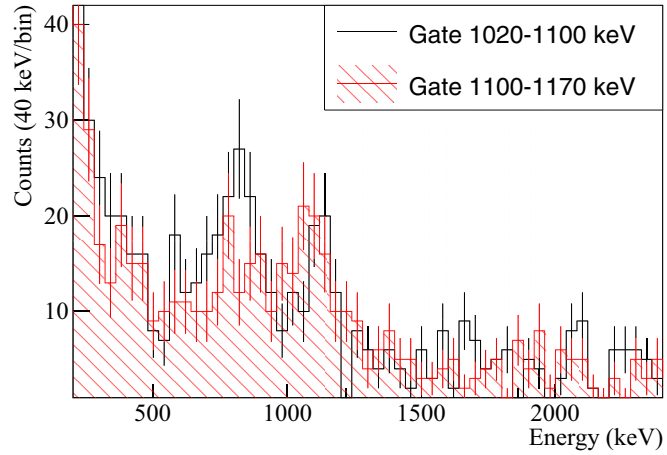


FIG. 3. Coincidence spectra for $^{72}$Ni. The events in the gate between 1020 and 1100 keV shows a clear coincidence with the $4_1^+ \rightarrow 2_1^+$ transition, while the gate on 1100–1170 keV only shows events in coincidences with the $2_1^+ \rightarrow 0_{gs}^+$ transition, suggesting the population of the $2_2^+$ state.

To take into account possible feeding from this transition, 50% feeding was assumed and the error bar was calculated in order to account for the extreme cases of no feeding and 100% feeding. The line at around 5000 keV fitted for both spectra does not correspond to any known transition, and in the present study we limit its interpretation to the consideration of its possible feeding to the $2_1^+$ state. In this case, such feeding was taken into account in the same way as for the possible $3^-$ states. The possible feeding contributions mentioned above were taken into account in the size of the experimental uncertainties.

Exclusive cross sections were calculated based on the number of $\gamma$ rays in each transition after the feeding corrections and the number of incoming ions. Besides the statistical uncertainty given by the fit and the number of incident ions, the systematic uncertainty in the calculated cross sections include 2% due to the background selection, 6% for the simulated efficiency of DALI2, and 2% uncertainty in the target thickness. For $^{72}$Ni, values of 2.2(7) mb and 0.8(1) mb were obtained for the cross sections to populate the $2_1^+$ and $4_1^+$ states, respectively. For the same states in $^{74}$Ni, values of 2.7(10) mb and 0.6(2) mb were extracted. The cross section to populate the $2_2^+$ state was determined as 0.7(3) mb for $^{72}$Ni and 0.9(5) mb for $^{74}$Ni. For the possible $3^-$ states cross sections of 0.3(1) mb and 0.6(2) mb were determined, and for the transitions at 5000 keV values of 0.1(1) mb and 0.2(1) mb were evaluated for $^{72}$Ni and $^{74}$Ni, respectively.

Figure 4 shows the Doppler corrected $\gamma$-ray spectra obtained for $^{76}$Zn, together with its partial level scheme. The $2_1^+ \rightarrow 0_{gs}^+$ transition at 593(10) keV and the $4_1^+ \rightarrow 2_1^+$ transition at 708(16) keV, in agreement with the known values, were observed.

The simulated response of DALI2 to the $2_1^+ \rightarrow 0_{gs}^+$ transition (solid red line) and the $4_1^+ \rightarrow 2_1^+ \rightarrow 0_{gs}^+$ cascade (solid green line) were fitted, together with the double exponential function to model the background. No additional transition was required to accurately fit the spectrum. Cross sections of 1.9(10) mb and 1.3(6) mb were obtained for the $2_1^+$ and $4_1^+$

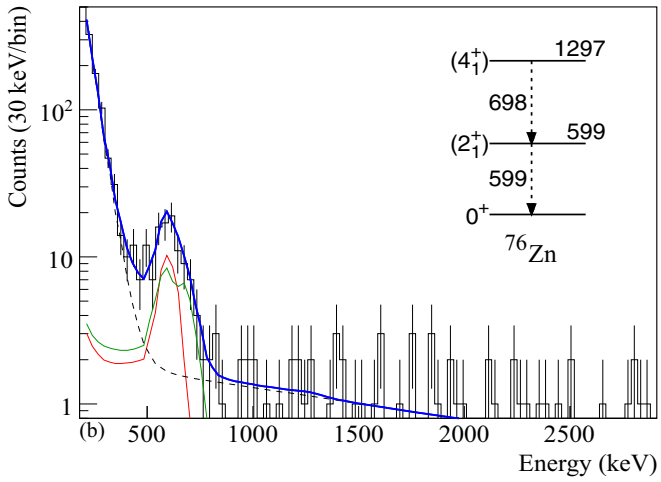


FIG. 4. Doppler-corrected spectra obtained for $^{76}$Zn. The spectrum was fitted by the convolution of the simulated response of DALI2 to the $2_1^+ \rightarrow 0_{gs}^+$ transition (solid red line) and the $4_1^+ \rightarrow 2_1^+ \rightarrow 0_{gs}^+$ cascade (solid green line) and a double exponential function which models the background (long dashed black line). Levels and decay energies are taken from Ref. [43]. See text for details.

states, respectively. The large uncertainties arise from the low statistics for this isotope.

Figure 5 shows the spectra obtained for $^{80}$Zn. In order to limit the atomic background at low energies, only detectors at forward angles were considered. A peak at 1487(8) keV, consistent with the previously reported $2_1^+ \rightarrow 0_{gs}^+$ transition [30], was observed, as well as a peak at 487(3) keV, which corresponds to the recently reported $4_1^+ \rightarrow 2_1^+$ transition [45].

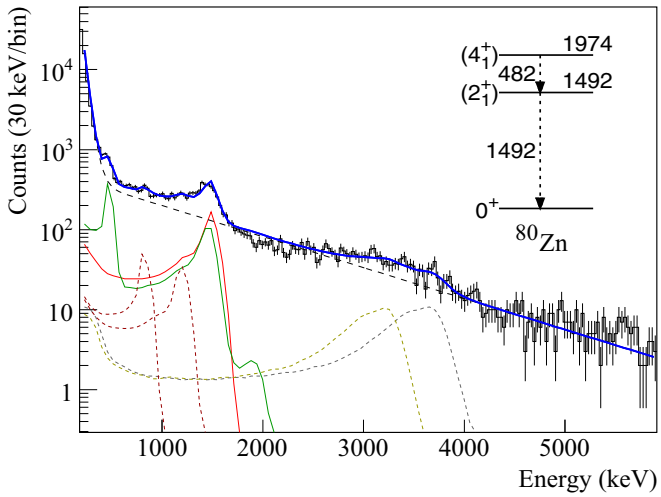


FIG. 5. Doppler corrected spectra obtained for $^{80}$Zn. The spectrum was fitted by the convolution of the simulated response of DALI2 to the $2_1^+ \rightarrow 0_{gs}^+$ transition (solid red line) and the $4_1^+ \rightarrow 2_1^+ \rightarrow 0_{gs}^+$ cascade (solid green line) and a double exponential function which models the background (long dashed black line). Two previously reported transitions (dashed dark red lines) and two high-energy transitions (dashed lines) were used to obtain a better fit to the data. Levels and decay energies are taken from Ref. [45]. See text for details.

TABLE II. Inelastic proton-scattering cross section to populate the $2_1^+$ and $4_1^+$ states deduced for $^{72,74}$Ni and $^{76,80}$Zn in the present work. The values obtained for the $2_2^+$ state are also listed for $^{72,74}$Ni. Cross sections obtained using a microscopic JLM/QRPA calculation are also presented. Such values correspond to an average over the energy of the beam before and after the target to take into account the energy loss.

| Cross section (mb) | $^{72}$Ni | $^{74}$Ni | $^{76}$Zn | $^{80}$Zn |
|---|---|---|---|---|
| $\sigma_{2_1^+}$ (expt) | 2.2(7) | 2.7(10) | 1.9(10) | 1.3(3) |
| $\sigma_{2_1^+}$ (theo) | 1.42 | 1.56 | — | 2.01 |
| $\sigma_{4_1^+}$ (expt) | 0.8(1) | 0.6(2) | 1.3(6) | 1.1(2) |
| $\sigma_{4_1^+}$ (theo) | 0.31 | 0.29 | — | 0.46 |
| $\sigma_{2_2^+}$ (expt) | 0.7(3) | 0.9(5) | — | — |
| $\sigma_{2_2^+}$ (theo) | 0.60 | 0.65 | — | 0.15 |

The response of DALI2 to the $2_1^+ \rightarrow 0_{gs}^+$ transition (solid red line) and to the $4_1^+ \rightarrow 2_1^+ \rightarrow 0_{gs}^+$ cascade (solid green line) were taken into account for the fit. For the case of the $4_1^+ \rightarrow 2_1^+$ transition, the half-life of $136^{+92}_{-67}$ ps reported by Ref. [45], was included. Previously reported transitions at 841 keV and 1195 keV [45] were used in the fit (dashed dark red lines). These transitions are reported to feed the $4_1^+$ state, and therefore they were not considered to directly feed the $2_1^+$ state. Two high-energy transitions, at 3280(20) and 3690(30) keV, were necessary to obtain a better description of the spectrum. The origin of these lines could not be determined, and in this analysis we only consider their possible feeding to the $2_1^+$ state. As for the case of the Ni isotopes, 50% feeding was assumed. Values of 1.3(3) mb and 1.1(2) mb for the population of the $2_1^+$ and $4_1^+$ states were obtained, respectively. For the two high-energy transitions, cross sections of 0.3(1) mb and 0.2(1) mb were measured. The observed cross sections for the $2_1^+$, $4_1^+$, and $2_2^+$ states are summarized in Table II.

## IV. ANALYSIS

The cross sections measured in the present work were analyzed considering two reaction models. First, a microscopic approach, based on transition densities obtained from quasiparticle random-phase approximation (QRPA) and the Jeukenne-Lejeune-Mahaux (JLM) potential [46], was used to calculate inelastic-scattering cross sections. Theoretical results were compared to experimental findings to infer neutron to proton matrix element ratios. Next, deformation lengths for the first quadrupole excitation were determined using the phenomenological collective model for nucleon scattering and compared to deformations previously reported for lighter Ni and Zn isotopes.

### A. Microscopic model for inelastic scattering

The measured cross sections were compared to calculations from a microscopic reaction model based on the JLM folding method [46]. The JLM model relies on a finite-range two-body effective interaction inferred from a Brueckner-Hartree-Fock (BHF) optical potential calculation in nuclear matter for

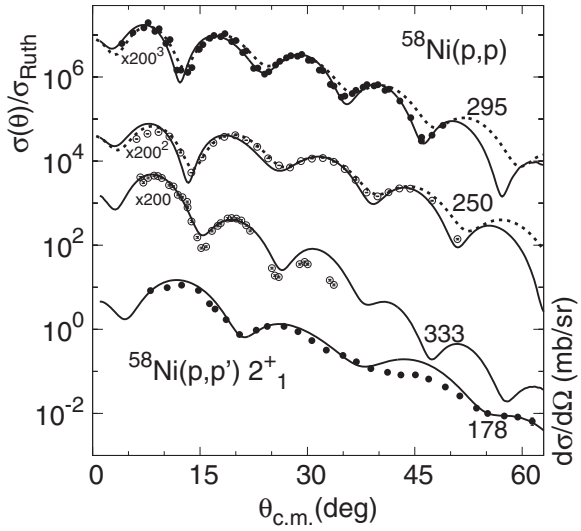


FIG. 6. Proton scattering on $^{58}$Ni. The two top curves show ratios of differential elastic-scattering cross sections to the Rutherford cross sections (left $y$ axis). The two bottom curves show differential cross sections for direct inelastic scattering to the $2^+_1$ state (right $y$ axis). Full black curves are calculated with the reaction model described in Sec. IV A. Dashed curves are calculations from the KD02 potential. Incident energies are specified in the plot in MeV. Experimental data are from Refs. [52–54] for elastic scattering and from Refs. [55–57] for inelastic scattering. Cross sections are scaled by the factors indicated in the plot.

nucleon incident energies up to 160 MeV. This interaction is folded with nuclear matter densities, measured or obtained from nuclear structure approaches, to obtain local optical potentials for finite nuclei. These complex potentials contain a central part, with isoscalar and isovector components, and an ad hoc spin-orbit potential. A common procedure consists in multiplying each term of this potential with a factor $\lambda$, which remains close to unity, in order to fit elastic-scattering observables. In 2001, Bauge *et al.* [47] provided a global parametrizaion of these $\lambda$ factors, as functions of target mass and incident energy, that reproduces both proton and neutron elastic and quasi-inelastic-scattering observables for energies ranging from $E = 1$ keV to 200 MeV and target nuclei with mass in the range $A = 40$–209. This JLM folding model has then been intensively and successfully used to interpret many nucleon inelastic-scattering data for energies up to 200 MeV in a DWBA or coupled-channels framework using transition densities stemming, for instance, from (Q)RPA calculations [48–50].

In the present work, the average energy of the beam in front of the target was ≈270 MeV and the energy at the target exit was around 200 MeV. To treat such high energies, an empirical procedure was devised to obtain an effective two-body interaction within a folding procedure equivalent to that of the JLM model by extrapolating the components of the JLM potential up to 340 MeV. The procedure for extracting the various components of the BHF of the JLM model will be fully explained in a forthcoming article [51]. Figure 6 shows a sample of the results obtained for the elastic scattering of $^{58}$Ni at 250 MeV and 295 MeV, as well as the inelastic scattering to the $2^+_1$ state for $^{58}$Ni at 178 and 333 MeV. Experimental data are shown by the symbols, while the full black lines show the present calculations performed using the "extended"-JLM folding model. As can be seen from the plot, the extended calculation shows a good agreement with the experimental data and encourages us to use it for the present analysis.

Angular integrated inelastic-scattering cross sections for the various excitations of $^{72,74}$Ni and $^{80}$Zn have thus been extracted within this model using neutron and proton transition densities calculated with QRPA. Such calculations were based on the Gogny D1M force and were performed in a cylindrical harmonic oscillator basis with 11 major shells [58]. The calculations were limited to $^{72,74}$Ni and $^{80}$Zn, for which the underlying mean field displays a spherical or near-spherical symmetry. The extraction of accurate transition densities for deformed nuclei, such as $^{76}$Zn, would require further work. Cross sections were calculated for each isotope in the energy range indicated in Table I and averaged to account for the energy loss along the thick target. The obtained results are compared to experimental data in Table II.

The experimental cross sections for the $2^+_1$ state of $^{72,74}$Ni are slightly underpredicted by the model, while for the $2^+_1$ state in $^{80}$Zn, the model gives a value significantly higher than the experiment. A good agreement is found for the $2^+_2$ state of $^{72,74}$Ni, but the model systematically underestimates the cross sections for the $4^+_1$ state of the three isotopes. This last discrepancy is hard to interpret and may indicate that large uncertainties are associated to both the nuclear structure ingredients and to the procedure used to extract the experimental value of the cross section. Indeed, the QRPA model may need to be extended to account for two-phonon (four quasiparticles) excitations to properly represent the $4^+_1$ state. Besides, indirect feeding to the $4^+_1$ state may have been underestimated resulting in an overestimated experimental value of the cross section. Both of those aspects need to be fully understood before conclusions on this comparison can be provided. For the $2^+_1$ states, however, the QRPA approach, which considers a coherent sum of two quasiparticle states, is believed to include the relevant physics. Additionally, the uncertainties related to the indirect feeding are better controlled than for the $4^+_1$ state and have been taken into account to extract the experimental cross sections. Therefore, for the $2^+_1$ state, the disagreement between theory and experiment provides information on the accuracy of the neutron and proton transition densities used in the folding model.

The neutron (proton) matrix element is defined from the neutron (proton) radial transition density, $\rho_L^{n(p)}(r)$, as [59]

$$M_{n(p)} = \int \rho_L^{n(p)}(r) r^{L+2} dr. \quad (1)$$

The proton transition densities can be tested by comparing calculated and experimental reduced transition probabilities, $B(E2)\uparrow = (2L+1)M_p^2$. This comparison, displayed in Table III, shows a slight difference between the $B(E2)\uparrow$ calculated with QRPA and the experimental measurements. The reaction modeling can be corrected to take into account this

TABLE III. $B(E2)\uparrow$ values and $R_{N/Z} = (M_n/M_p)/(N/Z)$ for the isotopes of interest. For $B(E2)\uparrow$, the experimental value [28,29,60] as well as QRPA and LSSM prediction are displayed. For the $R_{N/Z}$, predictions using QRPA and LSSM calculations are shown together with the results obtained in the present work using the JLM/QRPA microscopic approach.

| | $^{72}$Ni | $^{74}$Ni | $^{80}$Zn |
|---|---|---|---|
| $B(E2)\uparrow$ (QRPA)($e^2$ fm$^4$) | 453 | 482 | 984 |
| $B(E2)\uparrow$ (LSSM)($e^2$ fm$^4$) | 598.2 | 540.7 | 934.7 |
| $B(E2)\uparrow$ (exp)($e^2$ fm$^4$) | 370(50) | $642^{+216}_{-226}$ | 730(90) |
| $R_{N/Z}$(QRPA) | 1.13 | 1.15 | 0.80 |
| $R_{N/Z}$(LSSM) | 1.085 | 1.086 | 0.435 |
| $R_{N/Z}$(JLM/QRPA) | 1.80(57) | $1.40^{+0.85}_{-0.55}$ | 0.72(31) |

difference by scaling $M_p$ with the a factor

$$f_p = \sqrt{\frac{B(E2)\uparrow(\text{exp})}{B(E2)\uparrow(\text{QRPA})}}. \quad (2)$$

After scaling $M_p$, the value of $M_n$ can be scaled by a factor $f_n$, selected to reproduce the experimental cross section. This procedure was performed for all the isotopes of interest. In this way, reevaluated values of $M_n/M_p$ and of the ratio

$$R_{N/Z} = \frac{M_n/M_p}{(N/Z)} \quad (3)$$

were extracted from the microscopic JLM calculation, the experimental $B(E2)\uparrow$ values, and the measured cross sections. Table III compares the values of $R_{N/Z}$ predicted by QRPA and the ones obtained from the scaling procedure, $R_{N/Z}(\text{JLM/QRPA}) = (f_n/f_p)R_{N/Z}(\text{QRPA})$. The error bars associated to $R_{N/Z}$ (JLM/QRPA) account for the reported errors of $B(E2)\uparrow$ in the normalization of $M_p$ and the subsequent changes of $M_n$. These values will be discussed in Sec. V.

### B. Deformation in the collective model

The deformation length of each isotope, $\delta_{(p,p')}$, was obtained from the measured cross section using the nuclear reaction code ECIS-97 [61,62]. The calculations included a first-order, harmonic vibrational model implemented with the KD02 global optical potential [63]. This potential is based on a large set of measurements of stable isotopes with beam energies up to 200 MeV/nucleon. However, the smooth variation of the model parameters in the energy range 150–200 MeV permit the assumption that the KD02 potential can be safely extrapolated at energies up to a few tens of MeV beyond 200 MeV. As it is shown in Fig. 6, the results obtained with this potential for proton elastic scattering on $^{58}$Ni at energies beyond 200 MeV (dashed curves) provide a good description of experimental angular distributions. The KD02 potential was thus considered suitable for the present study, although a careful check of its pertinence for energies beyond 200 MeV and exotic isotopes is still required.

From the resulting deformation lengths, a deformation parameter $\beta_2(p,p')$ was obtained using the relation $\delta_{(p,p')} = \beta_2(p,p')R$, where $R = 1.2A^{1/3}$. As the protons in the target interact with all the nucleons of the projectile, $\beta_2(p,p')$ represents the matter deformation. Measurements using electromagnetic (EM) probes, such as Coulomb excitation, are only sensitive to the protons and therefore would yield a charge deformation, $\beta_2$(EM). In that case deformations can be deduced from the $B(E2)\uparrow$ value as

$$\beta_2(\text{EM}) = \frac{4\pi}{3ZeR^2}\sqrt{B(E2)\uparrow}. \quad (4)$$

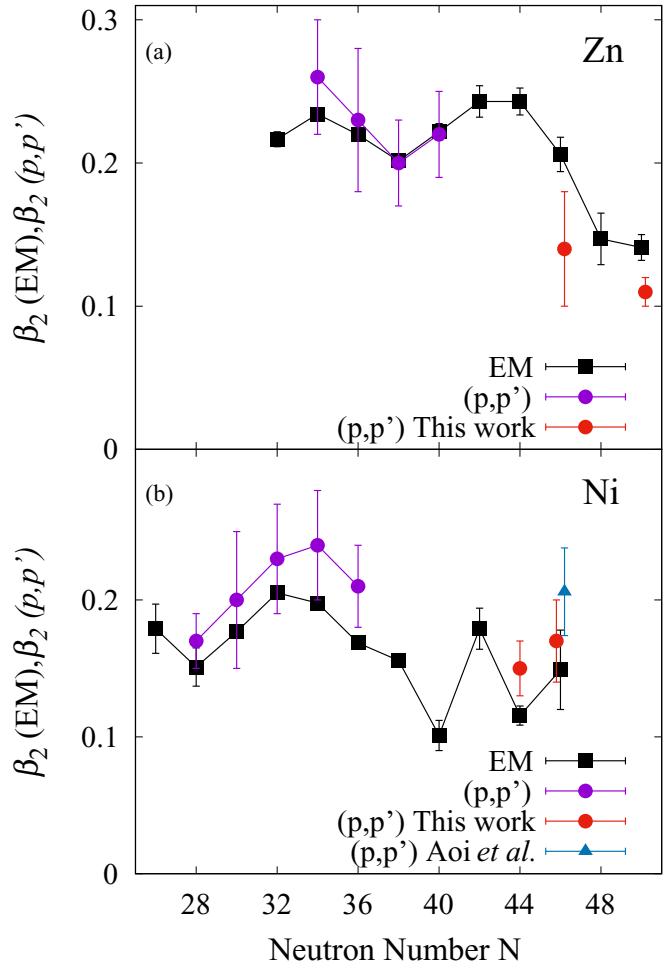


FIG. 7. Adopted values for the deformation parameter $\beta_2$(EM) [28,60] as a function of neutron number and $\beta_2(p,p')$ obtained using proton inelastic scattering for (a) Zn isotopes and (b) Ni isotopes. The red full circles are the results of the present work. The filled triangle corresponds to a previous measurement at 80 MeV/nucleon [64]. The purple circles represent an average of previous measurements [56,65–76].

Figure 7 shows the adopted values of $\beta_2$(EM) [28,60] as a function of neutron number for even-even Ni and Zn isotopes, along with the deformation parameters $\beta_2(p,p')$ extracted from this work.

For the Ni isotopes, the values obtained for the matter deformation are slightly higher than $\beta_2$(EM), although for $^{74}$Ni the values agree within error bars. For $^{74}$Ni, our estimated deformation agrees with the value obtained from a previous experiment performed at 80 MeV/nucleon and analyzed within the collective model [64], as shown by the blue triangle in the figure. The increased matter deformation compared to the

charge deformation is consistent with the results obtained from previous measurements in lighter Ni isotopes, as shown by the purple points in the figure. These points represent the average of different available results [56,65–76] with the error bar calculated as the standard deviation of the measurements added in quadrature with the error of individual measurements, when reported.

For the the case of the Zn isotopes, the present measurements are below $\beta_2$(EM). Previous measurements on stable Zn isotopes [66,70,72,74,75,77–83] show similar values of $\beta_2$(EM) and $\beta_2(p,p')$ for $^{68,70}$Zn and hint at a small increase on $\beta_2(p,p')$ for $^{64,66}$Zn.

## V. DISCUSSION

In the collective model for vibration, the nucleus is modeled as a homogeneous proton-neutron fluid. This implies that (i) proton and neutron densities have the same deformation, (ii) $M_n/M_p = N/Z$, and (iii) $\beta_2(p,p')$ remains close to $\beta_2$(EM).

The systematic enhancement of $\beta_2(p,p')$ over $\beta_2$(EM) has been reported for stable proton-closed-shell isotopes [84] and can be related to the significance of the contribution of the neutrons to the collectivity of such nuclei. As illustrated in Fig. 7, this behavior seems to be maintained for neutron-rich Ni isotopes. This suggests that in this region of the nuclear chart, the Ni isotopes still behave as proton-closed-shell isotopes, which in turn indicates the conservation of the $Z = 28$ gap. For the case of $^{80}$Zn, with $N = 50$, $\beta_2(p,p')$ turns out to be lower than $\beta_2$(EM). This results is in line with an increased contribution of the protons to the collectivity. An equivalent behavior has been observed for stable neutron-closed-shell isotopes [84] and is consistent with the conservation of the $N = 50$ magic number in the vicinity of $^{78}$Ni. However, it is pointed out that the results obtained using the first-order vibrational model have to be interpreted with care, since the validity of this model for very neutron-rich isotopes has not been definitively established. Moreover, various kinds of reaction model analysis were used to extract to $\beta_2(p,p')$ values from previous works reported in Fig. 7. This could lead to very different systematic uncertainties that are not always quoted completely. To ensure the validity of the information inferred from the comparison of various $\beta_2(p,p')$ values, the exact same reaction model should be used to extract $\beta_2$ from the various $(p,p')$ cross sections. Such a work, is beyond the scope of the present paper.

In Sec. IV A, values of $R_{N/Z}$ were obtained from a microscopic reaction model calculation, based on the QRPA nuclear structure approach, constrained by both experimental reduced transition probabilities, and the experimental proton inelastic-scattering cross sections from the present work. As shown in Table III, the results obtained for $^{72,74}$Ni, labeled $R_{N/Z}$(JLM/QRPA), indicate that $M_n/M_p > N/Z$. In spite the large error bars, these results point to the fact that for the Ni isotopes, the $M_n/M_p = N/Z$ assumption of the collective model for vibration is not valid and that the contribution of the neutrons to the collectivity is more significant than the one of the protons. For $^{80}$Zn, the ratio $M_n/M_p$ is lower than $N/Z$, indicating the increased role of the protons to the collectivity of this nucleus. This analysis is rooted in a microscopic reaction model which takes all nuclear structure details into account. Therefore, it allows us to draw firmer conclusions on the respective neutron and proton contributions to the collectivity.

The predictions from the QRPA model, labeled $R_{N/Z}$(QRPA) in Table III, are in agreement within error bars with the previous conclusions. However, the deviation of $R_{N/Z}$ from unity of these predictions is weaker than the one shown by $R_{N/Z}$(JLM/QRPA) if the mean values are considered. From a nuclear structure point of view, this reveals that the neutron-to-proton collectivity ratio may be underpredicted within the present QRPA model.

Reduced transition probabilities and matrix elements ratios obtained with QRPA were also compared to results from large scale shell model (LSSM) calculations. Values of $R_{N/Z}$ predicted within this model, as well as the corresponding $B(E2)\uparrow$ value, are displayed in Table III. For this calculation, an effective interaction based on a $G$-matrix obtained from a realistic nucleon-nucleon interaction, modified with an empirical correction of the monopole part was employed, together with effective charges of $e_p = 1.31$ and $e_n = 0.46$ [85]. For the Ni isotopes, calculations were performed using a $^{48}$Ca core and considering the full $pf$ shell for protons and the $0f_{5/2}$, $1p_{3/2}$, $1p_{1/2}$, $0g_{9/2}$, and $1d_{5/2}$ orbits for neutrons [86]. For the Zn isotopes, the model space considered a $^{60}$Ca core, the full $pf$ shell for protons, and the full $sdg$ shell for neutrons [21]. It is pointed out that with the interaction used in the LSSM approach the magicity of $^{78}$Ni is preserved, although shape coexistence is predicted for this region [21].

For the Ni isotopes, the predictions of QRPA and LSSM for $R_{N/Z}$ differ by less than 6%. In the case of $^{80}$Zn, $R_{N/Z}$(LSSM) is a factor 0.54 smaller than $R_{N/Z}$(QRPA). This indicates that the LSSM neutron matrix element is roughly half of the QRPA one. In spite of these differences, both models predict an increased role of neutrons to the collectivity of the Ni isotopes, and of the protons in the case of $^{80}$Zn, although the mean values of $R_{N/Z}$(JLM/QRPA) are still not reproduced. Such behavior indicates that the neutron-to-proton collectivity ratio is not accurately predicted by the theoretical models; however, the large uncertainties associated to the measured cross sections prevent firmer conclusions on the accuracy of nuclear structure calculations.

Extracting properties of isotopes in the region around $^{78}$Ni presents different challenges for the theoretical models as well as for the experimental measurements. A first step towards the determination of $R_{N/Z}$ was undertaken within this work. In the future, high accuracy $B(E2)\uparrow$ as well as proton inelastic-scattering measurements are desired to reveal the underlying physics and to help improving nuclear structure modeling.

## VI. SUMMARY

We have studied the evolution of $2_1^+ \rightarrow 0_{gs}^+$ transition matrix elements around $^{78}$Ni by means of proton inelastic scattering on $^{72,74}$Ni and $^{76,80}$Zn in inverse kinematics at energies above 200 MeV/nucleon. Direct proton inelastic-scattering cross sections to the $2_1^+$ and $4_1^+$ states were derived from the $\gamma$-ray spectrum of each isotope. For $^{72,74}$Ni, the $(p,p')$ cross section for a possible $2_2^+$ state was also measured. An extension of the JLM folding model above 200 MeV/nucleon was developed

for the first time. This model, together with nucleon matter densities from QRPA was used to analyze the measured cross sections of the $2_1^+$ state of $^{72,74}$Ni and $^{80}$Zn to obtain $M_n/M_p$ values. The results suggest that for the Ni isotopes $(M_n/M_p) > (N/Z)$, which implies that the contribution of the neutrons to the collectivity is enhanced. For $^{80}$Zn, the calculation yields $(M_n/M_p)/(N/Z) < 1$, which is in agreement with an increased role of the protons to the collectivity. Deformation lengths obtained within a vibrational model as well as large-scale shell-model calculations support these findings. The observed behavior of the Ni isotopes is consistent with the conservation of the $Z = 28$ gap for neutron-rich Ni isotopes. In turn, the results for $^{80}$Zn suggest that the shell closure for $N = 50$ is conserved when approaching $Z = 28$.

Studies on proton inelastic scattering in inverse kinematics at high energies have become available thanks to the improvements on the intensity of radioactive ion beam facilities. Due to the high energies and large isospin values, the interpretation of the data becomes challenging and demands new theoretical tools. In this work, a step towards a consistent interpretation of the $(p, p')$ data has been undertaken, which will be beneficial for the analysis of future proton inelastic-scattering data and to the extraction of useful physics parameters linked to nuclear structure calculations.

## ACKNOWLEDGMENTS

The authors are thankful to the accelerator and BigRIPS teams for stable operation, high intensity of the uranium primary beam, and production of secondary beams during the experiment. Fruitful discussion with N. Van Giai and A. Severyukhin are acknowledged. MINOS has been supported by the European Research Council through the ERC Grant No. MINOS-258567. A.O. has been supported by the JSPS long-term fellowship L-13520 at the RIKEN Nishina Center. C.S. has been supported by the IPA program at the RIKEN Nishina Center. L.X.C. has been supported by the Ministry of Science and Technology of Vietnam through the Physics Development Program Grant No. ĐTĐLCN.25/18. M.L.C. and V.W. further acknowledge support through the German BMBF Grants No. 05P12RDFN8 and No. 05P15RDFN1. The experiment and the data analysis have been supported by the Helmholtz International Center for FAIR funded by the State of Hesse within its LOEWE initiative.

[1] O. Sorlin and M.-G. Porquet, Prog. Part. Nucl. Phys. **61**, 602 (2008).
[2] A. Gade *et al.*, Phys. Rev. C **74**, 021302 (2006).
[3] F. Wienholtz *et al.*, Nature **498**, 346 (2013).
[4] D. Steppenbeck *et al.*, Nature **502**, 207 (2013).
[5] R. F. Garcia Ruiz *et al.*, Nat. Phys. **12** (2016).
[6] A. Ozawa, T. Kobayashi, T. Suzuki, K. Yoshida, and I. Tanihata, Phys. Rev. Lett. **84**, 5493 (2000).
[7] A. Obertelli *et al.*, Phys. Lett. B **633**, 33 (2006).
[8] R. Kanungo *et al.*, Phys. Rev. Lett. **102**, 152501 (2009).
[9] A. Navin *et al.*, Phys. Rev. Lett. **85**, 266 (2000).
[10] H. Iwasaki *et al.*, Phys. Lett. B **481**, 7 (2000).
[11] H. Iwasaki *et al.*, Phys. Lett. B **491**, 8 (2000).
[12] S. Shimoura *et al.*, Phys. Lett. B **560**, 31 (2003).
[13] C. Détraz D. Guillemaud, G. Huber, R. Klapisch, M. Langevin, F. Naulin, C. Thibault, L. C. Carraz, and F. Touchard, Phys. Rev. C **19**, 164 (1979).
[14] T. Motobayashi *et al.*, Phys. Lett. B **346**, 9 (1995).
[15] B. Bastin *et al.*, Phys. Rev. Lett. **99**, 022503 (2007).
[16] S. Takeuchi *et al.*, Phys. Rev. Lett. **109**, 182501 (2012).
[17] B. Pfeiffer *et al.*, Nucl. Phys. A **693**, 282 (2001).
[18] K. Sieja and F. Nowacki, Phys. Rev. C **81**, 061303 (2010).
[19] T. Otsuka, T. Suzuki, R. Fujimoto, H. Grawe, and Y. Akaishi, Phys. Rev. Lett. **95**, 232502 (2005).
[20] K. T. Flanagan *et al.*, Phys. Rev. Lett. **103**, 142501 (2009).
[21] F. Nowacki, A. Poves, E. Caurier, and B. Bounthong, Phys. Rev. Lett. **117**, 272501 (2016).
[22] W. Pinkston and G. Satchler, Nucl. Phys. **27**, 270 (1961).
[23] L. A. Riley *et al.*, Phys. Rev. C **72**, 024311 (2005).
[24] C. Campbell *et al.*, Phys. Lett. B **652**, 169 (2007).
[25] L. A. Riley *et al.*, Phys. Rev. C **90**, 011305 (2014).
[26] O. Sorlin *et al.*, Phys. Rev. Lett. **88**, 092501 (2002).
[27] O. Perru *et al.*, Phys. Rev. Lett. **96**, 232501 (2006).
[28] K. Kolos *et al.*, Phys. Rev. Lett. **116**, 122502 (2016).
[29] T. Marchi *et al.*, Phys. Rev. Lett. **113**, 182501 (2014).
[30] J. Van de Walle *et al.*, Phys. Rev. Lett. **99**, 142501 (2007).
[31] J. Van de Walle *et al.*, Phys. Rev. C **79**, 014309 (2009).
[32] T. Kubo *et al.*, Progr. Theor. Exp. Phys. **2012** (2012).
[33] J. Daugas *et al.*, Phys. Lett. B **476**, 213 (2000).
[34] A. Obertelli *et al.*, Eur. Phys. J. A **50**, 8 (2014).
[35] C. Santamaria *et al.*, Phys. Rev. Lett. **115**, 192501 (2015).
[36] N. Paul *et al.*, Phys. Rev. Lett. **118**, 032501 (2017).
[37] S. Takeuchi *et al.*, Nucl. Instrum. Methods A **763**, 596 (2014).
[38] S. Agostinelli *et al.*, Nucl. Instrum. Methods A **506**, 250 (2003).
[39] P. Doornenbal *et al.*, Phys. Rev. C **90**, 061302(R) (2014).
[40] H. Liu *et al.*, Phys. Lett. B **767**, 58 (2017).
[41] P. Doornenbal *et al.*, Phys. Rev. C **93**, 044306 (2016).
[42] O. Tarasov and D. Bazin, Nucl. Instrum. Methods B **266**, 4657 (2008).
[43] `http://www.nndc.bnl.gov/ensdf/`.
[44] A. I. Morales *et al.*, Phys. Rev. C **93**, 034328 (2016).
[45] Y. Shiga *et al.*, Phys. Rev. C **93**, 024320 (2016).
[46] J.-P. Jeukenne, A. Lejeune, and C. Mahaux, Phys. Rev. C **16**, 80 (1977).
[47] E. Bauge, J. P. Delaroche, and M. Girod, Phys. Rev. C **63**, 024607 (2001).
[48] A. Corsi *et al.*, Phys. Lett. B **743**, 451 (2015).
[49] M. Dupuis *et al.*, Eur. Phys. J. A **51**, 168 (2015).
[50] M. Dupuis and E. Bauge, Eurphys. J. Web Conf. **122**, 06001 (2016).
[51] M. Dupuis (unpublished).
[52] H. Takeda, Memoirs Faculty of Sci., Kyoto Univ., Ser. Phys. **44**, 1 (2003).
[53] H. Sakaguchi, H. Takeda, S. Toyama, M. Itoh, A. Yamagoshi, A. Tamii, M. Yosoi, H. Akimune, I. Daito, T. Inomata, T. Noro, and Y. Hosono, Phys. Rev. C **57**, 1749 (1998).
[54] J. Zenihiro, H. Sakaguchi, T. Murakami, M. Yosoi, Y. Yasuda, S. Terashima, Y. Iwao, H. Takeda, M. Itoh, H. P. Yoshida, and M. Uchida, Phys. Rev. C **82**, 044611 (2010).

[55] N. M.Hintz, D. Cook, M. Gazzaly, M. A. Franey, M. L. Barlett, G. W. Hoffmann, R. Fergerson, J. McGill, G. Pauletta, R. L. Boudrie, J. B. McClelland, and K. W. Jones, Phys. Rev. C **37**, 692 (1988).
[56] A. Ingemarsson *et al.*, Nucl. Phys. A **365**, 426 (1981).
[57] A.Ingemarsson *et al.*, Nucl. Phys. A **322**, 285 (1979).
[58] S. Péru and M. Martini, Eur. Phys. J. A **50**, 88 (2014).
[59] A. Bernstein *et al.*, Phys. Lett. B **103**, 255 (1981).
[60] B. Pritychenko *et al.*, At. Data Nucl. Data Tables **107**, 1 (2016).
[61] J. Raynal, Phys. Rev. C **23**, 2571 (1981).
[62] J. Raynal (unpublished).
[63] A. Koning and J. Delaroche, Nucl. Phys. A **713**, 231 (2003).
[64] N. Aoi *et al.*, Phys. Lett. B **692**, 302 (2010).
[65] J. Dickens *et al.*, Phys. Lett. **6**, 53 (1963).
[66] J. Benveniste *et al.*, Phys. Rev. **133**, B323 (1964).
[67] A. L. McCarthy and G. M. Crawley, Phys. Rev. **150**, 935 (1966).
[68] S. F. Eccles *et al.*, Phys. Rev. **141**, 1067 (1966).
[69] P. Beuzit *et al.*, Nucl. Phys. A **128**, 594 (1969).
[70] C. M. Perey *et al.*, Phys. Rev. C **2**, 468 (1970).
[71] N. Lingappa and G. W. Greenlees, Phys. Rev. C **2**, 1329 (1970).
[72] M. Throop *et al.*, Nucl. Phys. A **283**, 475 (1977).
[73] G. Kyle *et al.*, Phys. Lett. B **91**, 353 (1980).
[74] E. Fabrici, S. Micheletti, M. Pignanelli, F. G. Resmini, R. DeLeo, G. D'Erasmo, and A. Pantaleo, Phys. Rev. C **21**, 844 (1980).
[75] M. A. Kennedy, P. D.Cottle, and K. W.Kemper, Phys. Rev. C **46**, 1811 (1992).
[76] G. Kraus *et al.*, Phys. Rev. Lett. **73**, 1773 (1994).
[77] V. Edwards, Nucl. Phys. A **101**, 17 (1967).
[78] V. Lewis *et al.*, Nucl. Phys. A **117**, 673 (1968).
[79] R. Johnson and G. Jones, Nucl. Phys. A **122**, 657 (1968).
[80] K. Yagi *et al.*, Nucl. Phys. A **132**, 690 (1969).
[81] W. Tait and V. Edwards, Nucl. Phys. A **203**, 193 (1973).
[82] J. Jabbour *et al.*, Nucl. Phys. A **464**, 260 (1987).
[83] J. Jabbour *et al.*, Nucl. Phys. A **464**, 287 (1987).
[84] A. M. Bernstein, V. R. Brown, and V. A. Madsen, Comments Nucl. Part. Phys. **11**, 203 (1983).
[85] M. Dufour and A. P. Zuker, Phys. Rev. C **54**, 1641 (1996).
[86] S. M. Lenzi, F. Nowacki, A. Poves, and K. Sieja, Phys. Rev. C **82**, 054301 (2010).